The Astrophysical Journal, 934:17 (8pp), 2022 July 20 https://doi.org/10.3847/1538-4357/ac7720

XMM-Newton and NuSTAR Observations of the Compact Millisecond Pulsar Binary PSR J1653–0158

Jane SiNan Long[1], Albert K. H. Kong[1], Kinwah Wu[2], Jumpei Takata[3], Qin Han[2,4], David C. Y. Hui[5], and Kwan Lok Li[6]
[1] Institute of Astronomy, National Tsing Hua University, Hsinchu 30013, Taiwan, Republic of China; sinan_jane@gapp.nthu.edu.tw, akong@phys.nthu.edu.tw
[2] Mullard Space Science Laboratory, University College London, Holmbury St Mary, Surrey, RH5 6NT, UK; kinwah.wu@ucl.ac.uk
[3] School of Physics, Huazhong University of Science and Technology, Wuhan, People's Republic of China
[4] School of Astronomy and Space Science, Nanjing University, Nanjing, 210023, People's Republic of China
[5] Department of Astronomy and Space Science, Chungnam National University, Daejeon, Republic of Korea
[6] Department of Physics, National Cheng Kung University, Tainan, Taiwan, Republic of China
Received 2021 September 2; revised 2022 June 4; accepted 2022 June 7; published 2022 July 21

Abstract

We have presented the first joint XMM-Newton and NuSTAR analysis of the millisecond pulsar (MSP) binary PSR J1653−0158. The 75 minute orbital period inferred from optical and gamma-ray observations together with the 1.97 ms pulsation in the gamma-rays indicate that this system is the most compact Black Widow MSP system known to date. The orbital period was not detected in the XMM-Newton and NuSTAR data, probably due to insufficient photon counts obtained in the observations. Fitting the joint X-ray spectrum of PSR J1653−0158 with a power law gives a photon index $\Gamma = 1.71 \pm 0.09$. The X-ray luminosity of the source in the (0.2–40) keV band is deduced to be 1.18×10^{31} erg s^{-1}, for an adopted distance of 0.84 kpc. We have shown that the broadband X-ray spectrum can be explained by synchrotron radiation from electrons accelerated in the intrabinary shock, and the gamma-rays detected in the Fermi data are curvature radiations from electrons and positrons in the pulsar magnetosphere. Our kinematic analysis of the Tidarren systems PSR J1653–0158 and PSR J1311–3430 indicates that the two Tidarren systems are likely to have originated in the Galactic disk.

Unified Astronomy Thesaurus concepts: Millisecond pulsars (1062); X-ray binary stars (1811); Gamma-ray sources (633)

1. Introduction

The Fermi-LAT source 4FGL J1653.6−0158 (= PSR J1653 −0158) was proposed as a gamma-ray emitting millisecond pulsar (MSP) binary, when a variable X-ray and optical source with a 75 minutes periodicity was found within the gamma-ray positional uncertainty (Kong et al. 2014; Romani et al. 2014). The subsequent detection of a 1.97 ms pulsation in the gamma-ray band confirmed its nature as a MSP (Nieder et al. 2020). Compact MSP binary systems with binary periods as short as that of PSR J1653−0158 would have a low-mass semidegenerate companion (see, e.g., Bhattacharya & van den Heuvel 1991; Iben et al. 1997; Chen et al. 2013; Jia & Li 2014; Hui et al. 2018). The deduced mass of $\sim 0.014\,M_\odot$ (Nieder et al. 2020) of the companion is above the critical mass limit $\sim 0.006\,M_\odot$ for dynamically stable mass transfer (see, e.g., Kiel & Taam 2013). With continuous ablation by the energetic particles and evaporation by the radiation from the MSP, the companion star may lose all its mass completely, leaving only an isolated MSP in the system (Kluzniak et al. 1988; Phinney et al. 1988; Ruderman et al. 1989; Faucher-Giguére & Kaspi 2006).

Compact MSP binaries exhibit two distinctive observational behaviors, by which they are classified into two groups, with names assigned after two spider families: the Redback (RB) and the Black Widow (BW; see, e.g., Chen et al. 2013; Roberts 2013). RBs are believed to be systems in the transition from/between accretion and rotation-powered phases. Their companions are mostly partially degenerate stars that are filling the Roche lobe or very close to filling the Roche lobe. The BW systems are characterized by the ablation of the highly degenerate companion. They are not powered by the accretion processes and therefore are not X-ray luminous. Although some compact MSP binaries can switch between being rotation powered and accretion powered (see, e.g., Papitto et al. 2013); depending on the relative sizes of the companion stars and their Roche lobes, they would eventually become persistently rotation powered. These systems would resemble the BW systems if the companions fail to regain contact with their critical Roche surfaces. The currently known RBs generally have companions with mass $M_c \gtrsim 0.1\,M_\odot$ (see, e.g., Hui & Li 2019). Compact MSP binaries with companion mass $M_c \lesssim 0.05\,M_\odot$ almost certainly belong to the BW group (see Fruchter et al. 1988; Stappers et al. 1996). Some studies (e.g., Chen et al. 2013) suggest that most RBs and BWs are descendants of different groups of systems, implying that most of the observed RBs are unlikely to have evolved from the BW, despite that RBs can switch off accretion permanently.

The detection of the millisecond gamma-ray pulsations in PSR J1653−0158 implies that the MSP is presently not accreting. The low luminosity of the X-rays, about 10^{31} erg s^{-1}, observed in the source (Kong et al. 2014) is consistent with no significant mass transfer within the system. This, together with the deduced low companion mass (Nieder et al. 2020), readily puts PSR J1653−0158 as a BW, with its pulsar emissions powered by the extraction of the rotational energy of the neutron star.

This paper reports the findings from a joint multiwavelength timing and spectral analysis of the XMM-Newton, NuSTAR, and Fermi observations of PSR J1653−0158. Section 2 presents the observational setups and Section 3 reports the temporal and spectral analyses. Section 4 discusses the results from the analysis. We adopted an intrabinary shock model to explain the observed broadband X-ray spectral properties, as well as a magnetosphere model (Takata et al. 2012) to explain the gamma-ray spectral behavior. The origin of PSR J1653−0158 and its related compact MSP binaries are also discussed.

2. Observations

2.1. NuSTAR

PSR J1653−0158 was observed by NuSTAR (Harrison et al. 2013) on 2017 May 29 for about 102 ks (ObsID 30201017002; PI: Kong). The data were processed with the NuSTAR Data Analysis Software NUSTARDAS (v1.9.6), using the calibration data from CALDB version 20200813. Procedures with standard parameters in the NuSTAR Data Analysis Software Guide[7] were adopted to clean and filter the event lists. The calibrated and cleaned event lists were processed with the tool `nupipeline` following standard procedures. The HEASoft tool `nuproducts` were used to construct the response matrices for each of the two focal plane modules, FPMA/B, and to produce images, light curves, and spectra of the source. The FPMA/B net counts were ∼118 counts and ∼78 counts, respectively.

In our analysis, the energy range was set to be 3−40 keV as there were almost no source photons above 40 keV. Images, light curves, and spectra of the target were derived from the data extracted from a circular region with a radius of 20″ centered at the X-ray position of PSR J1653−0158. An annulus region with a width of 40″and an inner radius of 20″centered at the source were used to derive the background photons. The spectra of the source from FPMA and FPMB observations were rebinned such that there were at least 10 counts in each spectral bin.

2.2. XMM-Newton

PSR J1653−0158 was observed by XMM-Newton on 2017 March 9 (ObsID: 0790660101; PI: Kong). The total exposure time was 53 ks, with data obtained from the EPIC (European Photon Imaging Camera) MOS1, MOS2, and pn charge-coupled device detectors. We followed the data analysis procedure detailed in the data analysis threads version 7.0 provided by SAS v19.0.[8] Due to the very low signal-to-noise ratio of MOS1 and MOS2 data, we only used pn data in this work. The pn camera has a good sensitivity below 3 keV, which compensates for the lack of sensitivity of NuSTAR in low energies, and hence provides an essential constraint for the soft X-rays in spectral analysis. The raw data (observation data files) were processed to be used with `xmmextractor` together with calibration data provided by the current calibration files. The pn event lists were further processed with the EPIC reduction meta-tasks `emproc` and `epproc`, respectively. To filter the EPIC event lists for flaring background, the 10–12 keV light curve was examined with the SAS tool `evselct` and filtered the flare by setting rate expression "RATE < = 0.4" The effective exposure time is ∼25 ks after background flaring filtering. The cleaned event lists were then used to produce the light curves and spectrum. The radius of the source is chosen as ∼10″, and an annulus region with a width of 30″and an inner radius of 15″centered at the source were used to derive the background photons. After background subtraction, the net counts for pn are ∼893 counts.

2.3. Fermi-LAT

The Fermi-LAT data (the latest version, P8R3) from 2008 August 4 to 2021 March 19 (spanning over 150 months) were analyzed using the `Fermitools`. The on-source data was extracted from a region of 20° radius centered at the 4FGL J1653.6−0158 position, (R.A., decl.) = (253.°408, −1.°97667), with energies between 100 MeV and 300 GeV. The tracker in the front and back sections of all the events were included, from which we selected `evtype = 3`, and filtered the data with an event class `evtclass = 128` assuming PSR J1653−0158 (=4FGL J1653.6−0158) as a point source. To avoid the gamma-ray contamination coming from the Earth's albedo, photons with zenith angles smaller than 90° were selected. Furthermore, the selection was restricted to high quality data in the time intervals (i.e., choosing DATA_QUAL > 0). Binned likelihood analysis was performed using the Fermi science tool `gtlike`. To eliminate the background distribution, a background emission model, which included the Galactic diffuse emissions (`gll_iem_v07.fits`) and the isotropic diffuse emissions (`iso_P8R3_SOURCE_V3_v01.fits`) given by the Fermi Science Support Center, was applied. To obtain the best-fitting spectral model for 4FGL J1653.6−0158, we applied the user contributed tool `make4FGLxml.py` that uses the spectral model from the 4FGL catalog (Abdollahi et al. 2020) to calculate the flux contribution of each source in the 20° radius region of interest centered at the 4FGL J1653.6−0158 position. The test statistics value obtained by the source model `PLSuperExpCutoff2` in 100 MeV to 300 GeV energies is 4643.61.

3. Temporal and Spectral Analysis

3.1. Temporal Behavior

PSR J1653−0158 has an orbital period of 0.0519 days shown in the optical (Kong et al. 2014; Romani et al. 2014), gamma-ray (Nieder et al. 2020), and possibly X-ray (Kong et al. 2014) wave bands. In a previous X-ray study, the 75 minutes orbital period found in the optical is marginally shown in the Chandra data (Kong et al. 2014). By using the larger collecting area of XMM-Newton, we investigated the X-ray modulation in detail. We also used NuSTAR to investigate the light curve in the hard X-ray region.

Figure 1 shows the XMM-Newton folded light curves in the 0.2–10 keV band with the gamma-ray epoch $T_{\rm asc}$ = MJD 56513.479171(8) and an orbital period of 0.0519447575 (4) days measured from Fermi gamma-ray observations (Nieder et al. 2020). To show the broadband X-ray variability, we also plotted the NuSTAR folded light curve (3–40 keV). Furthermore, we plotted the hardness ratio (H/S) between hard X-rays (10–40 keV) and soft X-rays (3–10 keV). We found no evidence for the 75 minutes orbital modulation in either XMM-Newton or NuSTAR data.

[7] https://heasarc.gsfc.nasa.gov/docs/nustar/analysis/nustar_swguide.pdf
[8] https://heasarc.gsfc.nasa.gov/docs/xmm/abc

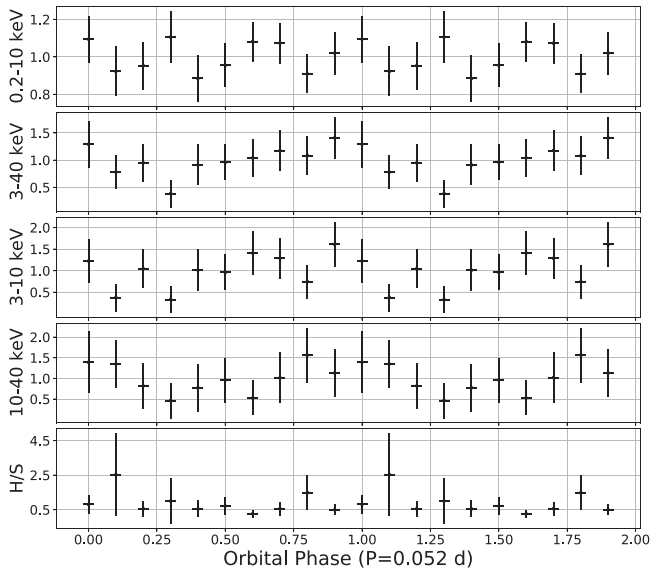

Figure 1. The folded light curves, in normalized counts, of PSR J1653–0158 from XMM-Newton (0.2–10 keV) and NuSTAR (3–40 keV) observations. Orbital cycles with different energy bands and hardness ratio (10−40 keV/3 −10 keV) are shown for clarity. The light curves do not show the 75 minutes orbital period.

The modulations in the light curves were assessed using the Lomb–Scargle periodogram (Lomb 1976; Scargle 1982). For the XMM-Newton normalized light curve, the Lomb–Scargle power at the 75 minutes orbital period corresponds to a 99% false alarm probability. A 3σ upper limit of 24% for the amplitude was obtained by fitting a sinusoidal function of the 75 minutes period. The false alarm probability is 3.7% and the 3σ upper limit for the amplitude is 80% for the NuSTAR light curve. The hardness ratio light curve is shown in Figure 1, for completeness, and it does not show evidence of spectral variations.

3.2. Spectral Properties

3.2.1. X-Ray

We used XSPEC version 12.11 to perform X-ray spectral fitting. Since both the NuSTAR and XMM-Newton observations were taken at similar epochs in 2017, we fitted the energy spectra from XMM-Newton, NuSTAR's FPMA and FPMB observations simultaneously to increase the signal-to-noise ratio. We also performed some simple spectral fits of individual spectra and they show no significant flux and spectral changes.

We employed different in-built models in XSPEC to perform spectral fitting. Based on previous X-ray study (Hui et al. 2015), we first tried an absorbed simple power-law model. In order to fit the spectra from the three cameras (pn and MOS1/2) of XMM-Newton and the two cameras of NuSTAR simultaneously, cross-calibration factors were taken into account in all the spectral models. In general, the 0.2−40 keV X-ray emissions can be well described with an absorbed power-law model ($\chi^2 = 51.35$ for 66 degrees of freedom (dof)) without obvious emission and absorption features (Figure 2). The best-fit absorption value is $(8.85 \pm 2.29) \times 10^{20}\,\mathrm{cm}^{-2}$, consistent with the extinction $A_V = 1.06$ obtained from light-curve modeling (Nieder et al. 2020), while the best-fit photon index is 1.71 ± 0.09. The unabsorbed 0.2−40 keV flux is $1.40^{+0.13}_{-0.12} \times 10^{-13}$ erg cm^{-2}s^{-1}, corresponding to an X-ray luminosity of 1.18×10^{31}erg s^{-1} at a distance of 0.84 kpc from optical modeling (Nieder et al. 2020).

Although an absorbed power-law model can provide a reasonable best fit, we also investigated if neutron star thermal emission from PSR J1653−0158 contributes part of the X-ray emissions (e.g., Kong et al. 2018). We included a nonmagnetic neutron star atmosphere component in the absorbed power-law model (nsatmos model in XSPEC; Heinke et al. 2006). We fixed the mass of the neutron star to be 2.17 $M_\odot$ (Nieder et al. 2020). Without losing generality, we adopted a value of 10 km as the radius of the neutron star (see Lattimer & Prakash 2001; Abbott et al. 2018). The effective temperature derived from the model is $7.99^{+4.02}_{-2.68} \times 10^5$ K and the unabsorbed flux in 0.2–40 keV is $6.27^{+0.35}_{-0.33} \times 10^{-14}$ erg cm^{-2}s^{-1}, corresponding to a luminosity of 5.29×10^{30} erg s^{-1} for a distance of 0.84 kpc. The best-fitting parameters from both spectral models are presented in Table 1. We applied a likelihood ratio test to test the validity of an extra component. A ratio of 0.988 suggests that a simple power-law model is sufficient. Furthermore, we used F-test to investigate if the additional neutron star atmosphere component is significant. The F-test probability is 0.0186 indicating that the additional component is not statistically required.

3.2.2. Gamma-Ray

For the GeV band, we divided the Fermi-LAT photon counts data into eight energy segments to obtain the gamma-ray spectrum (see blue crosses in Figure 3). We fitted the gamma-ray spectrum of PSR J1653−0158 with a power law and an exponential cutoff model:

$$\frac{dN}{dE} = N_0 \left(\frac{E}{E_0}\right)^{\Gamma} \exp(-aE^b), \quad (1)$$

where N is the photon counts per unit time, unit area, and E is the photon energy, N_0 and E_0 are the normalization factors, Γ is the spectral index, and a is the exponential factor. By setting $b = 2/3$ (an empirical value chosen for pulsars, see Abdollahi et al. 2020), $a = (8.4 \pm 0.74) \times 10^{-3}$ MeV$^{-\frac{2}{3}}$ and $\Gamma = 1.58 \pm 0.05$ were obtained. Note that the total flux is $F = (5.06 \pm 0.19) \times 10^{-8}$photons cm^{-2} s^{-1}.

4. Discussion

4.1. Theoretical Interpretation for the High-energy Emissions

We present an analysis of the broadband (0.2−40 keV) X-ray data of the compact BW PSR J1653−0158 obtained by XMM-Newton and NuSTAR. While the Chandra observation in the 0.3–8 keV energy band indicated a possible period of about 75 minutes (Kong et al. 2014), we found no clear modulation in the XMM-Newton and NuSTAR data. The null detection could be due to poorer photon statistics, as the point-spread functions of XMM-Newton and NuSTAR are much broader than that of Chandra. The background contribution of the XMM-Newton and NuSTAR light curves is 27% and 52%–65%, respectively. On the other hand, the background contribution is negligible (almost 0%) in the Chandra light curve.

Although a composite model, consisting of a power-law and a neutron star atmosphere component, fits the X-ray spectrum (up to about 40 keV) of PSR J1653−0158 well, a single component absorbed power-law model is sufficient. The

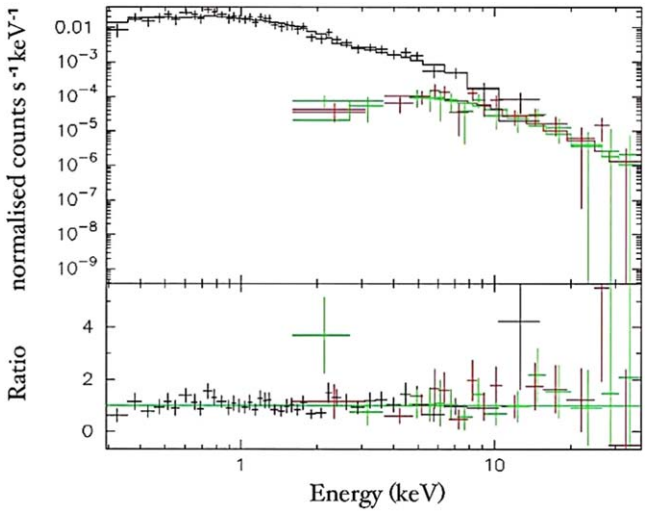

Figure 2. Model fit to the XMM-Newton (0.2–10 keV) and NuSTAR (3–40 keV) spectra of PSR J1653−0158. The best-fitting model is an absorbed power law with a photon index $\Gamma = 1.71$ (shown as the dark solid line).

Table 1
Spectral Fits for PSR J1653−0158.

Model	
Power law	
$N_{\rm H}$ (10^{20}cm^{-2})	8.85 ± 2.29
Γ	1.71 ± 0.09
$F_{0.2-40}$ (10^{-13} erg cm^{-2} s^{-1})	$1.40^{+0.13}_{-0.12}$
χ^2_ν/ dof	0.78/66
Power law + H atmosphere[a]	
$N_{\rm H}$ (10^{20}cm^{-2})	24.38 ± 14.31
Γ	1.60 ± 0.15
T(10^5K)	$7.99^{+4.02}_{-2.68}$
$F_{0.2-40}$ (10^{-14} erg cm^{-2} s^{-1})	$6.27^{+0.35}_{-0.33}$
χ^2_ν/dof	0.71/64

Note. Fluxes F are from combined XMM-Newton and NuSTAR unabsorbed flux and a distance of 0.84 kpc is assumed in calculations.
[a] The mass and radius of the neutron star were fixed to be 2.17 $M_\odot$ (Nieder et al. 2020) and 10 km, assuming a distance of 0.84 kpc.

parameters of $\Gamma = 1.71 \pm 0.09$ and $N_{\rm H} = (8.86 \pm 2.29) \times 10^{20}$ cm^{-2} obtained from the absorbed power-law fit is consistent with those obtained in the previous analysis of the Chandra observation (Kong et al. 2014; Romani et al. 2014). The photon index of $\Gamma = 1.71 \pm 0.09$ implies a spectral index $\alpha = 0.71 \pm 0.09$ (as $\alpha = \Gamma - 1$). If the X-rays are optically thin synchrotron radiation from nonthermal relativistic electrons with a power-law energy distribution, in a uniformed magnetized medium, we expect the power-law index of the electrons to be $p \approx 2.4$ (as $\alpha = (p-1)/2$) (see, e.g., Rybicki & Lightman 1986). Stochastic accelerations in shocks can produce energetic electrons with a power-law energy distribution ($p \approx 2.2-2.5$), in both relativistic and nonrelativistic regimes (see, e.g., Bell 1978; Achterberg et al. 2001). If the X-rays from PSR J1653−0158 are of synchrotron origin, then they could be emitted from energetic electrons accelerated in the bow shock formed when pulsar wind collided with stellar material ablated from the companion star. The existence of the ablating wind can also be inferred by optical observations, as indicated by the decreasing modulation and flat orbital minima

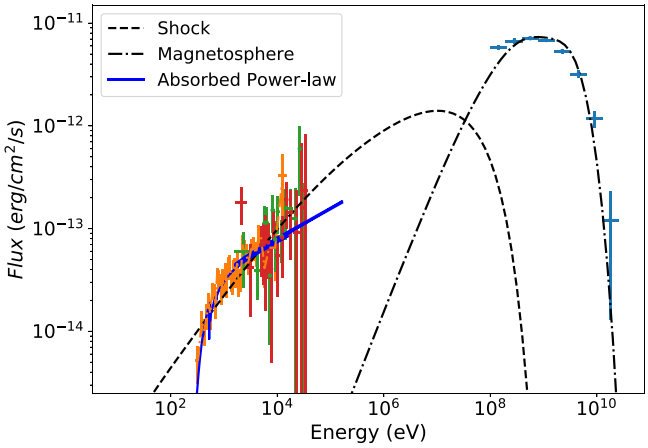

Figure 3. Broadband spectrum, in X-ray and gamma-ray energies, of PSR J1653−0158 fitted with an intrabinary shock and magnetosphere model (Takata et al. 2012). We assumed a momentum ratio of $\eta_b = 0.7$, a shocked pulsar wind velocity of $v \sim 0.25\,c$, and an inclination of 60°. The best-fit absorbed power-law model for the X-ray spectrum is also shown (thick blue curve).

in the blue colors. Optical light-curve modeling must include a nonthermal veiling flux component, which could be explained by synchrotron emission from an intrabinary shock (Romani et al. 2014; Nieder et al. 2020).

We considered an intrabinary shock and a magnetosphere model (Takata et al. 2012) to explain the general spectral behavior in the X-ray and gamma-ray bands. This intrabinary model was previously applied to explain the broadband high-energy spectrum of the RB system PSR J2129−0429 (Kong et al. 2018), which has a nondegenerate companion star. In PSR J2129−0429, the intrabinary shock has a momentum ratio of $\eta_{\rm b} \approx 7$ (where $\eta_{\rm b}$ is the ratio between the stellar magnetic pressure and the ram pressure of the pulsar wind). As the stellar wind dominated the flow, the intrabinary shock wrapped around the pulsar. In this study, we considered that the intrabinary shock in PSR J1653−0158 was produced by the collision of an isotropic pulsar wind with an envelope of material ablated from a white-dwarf (WD) companion. The intrabinary shock accelerated the electrons and positrons to relativistic energies and they emitted synchrotron X-rays. Different to PSR J2129−0429, the intrabinary shock in PSR J1653−0158 was located closer to the white-dwarf companion and wrapped around it. We adopted a magnetization parameter $\sigma = 0.1$, for the ratio of the magnetic energy and kinetic energy of the pulsar wind, and a momentum ratio $\eta_{\rm b} \approx 0.7$ in the model to fit the X-ray spectra of PSR J1653−0158. The pulsar wind carried out the spin-down power and was compressed by the shock. The shock provided a means to accelerate the charged electrons to relativistic energies, which emitted the synchrotron X-rays. Figure 3 shows the X-ray intrabinary model (dashed line) fit to the observed broadband X-ray spectrum.

The observed gamma-rays are not emitted from the high-energy electrons associated with the shock but are instead produced by the energetic charged particles in the pulsar magnetosphere (Cheng et al. 1986; Dyks & Rudak 2003; Watters et al. 2009). They are curvature radiation from relativistic electrons and positrons created through pair processes in the pulsar magnetosphere. This scenario provides an explanation to the double-peak features observed in the

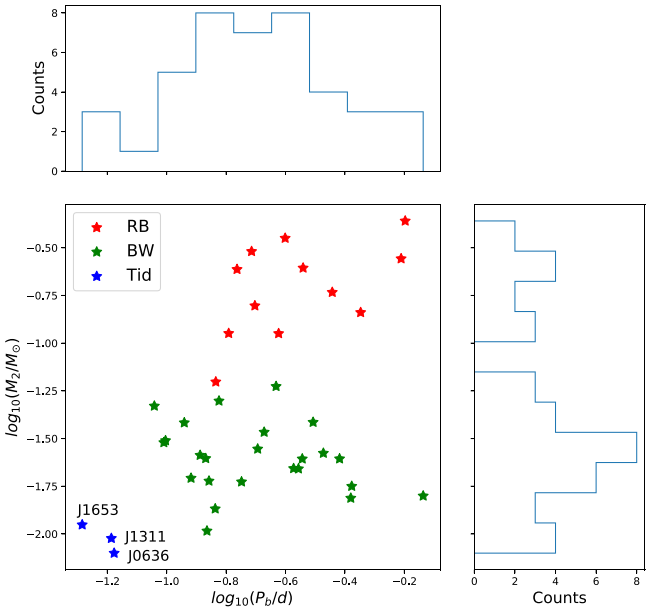

Figure 4. The distribution of eclipsing MSP binaries in the Galactic field are presented in the orbital period—companion mass plane. The BWs and RBs occupy two separate regions distinguished by the companion mass, while they are statistically indistinguishable by orbital period. The Tidarrens occupy the region visually well distinguishable from those resided in by the RBs and BWs, and they are separated from the other two groups by both the companion mass and the orbital period. The Tidarrens PSR J1653−0158, PSR J1311−3430, and PSR J0636+5129 are marked in blue and labeled, respectively.

gamma-ray light curves of MSP binaries (e.g., Huang et al. 2012; Li et al. 2014).

We applied a three-dimensional two-layer outer gap model of Wang et al. (2011) to calculate the gamma-ray spectrum of PSR J1653−0158. We estimated, from the spin period and the surface magnetic field, that the thickness of the outer gap is about 60% of the light cylinder radius. This indicates that the large fraction of the volume in the outer magnetosphere is occupied by the outer gap. We considered that the outer gap exists between the null charge surface of the Goldreich–Julian charge density and the light cylinder. This would produce a pulse profile consistent with the broad pulse profile as observed and also the high-efficiency ($L_\gamma/L_{\rm sd} \sim 66\%$) in the GeV energies (see Nieder et al. 2020). We assumed a value for the electric current corresponding to ≈50% of the Goldreich–Julian density and calculated the electric field along the magnetic field line. Figure 3 shows the spectrum of the curvature gamma-rays produced by our model,[9] together with the Fermi data.

4.2. Origin of PSR J1653−0158

We showed all spider MSP systems that have the characteristic eclipsing light curve in the Galactic field in Figure 4. The RBs and BWs are distinguished by their companion mass, whereas the subclass Tidarren (Tid) is distinguished from the main BW class by their companion mass as well as orbital period. The p-values resulting from the two-sample Kolmogorov–Smirnov tests between Tid and BWs are 2.7×10^{-3} for mass and 5.4×10^{-4} for period, indicating the differences between the two classes.

PSR J1653−0158 and two other compact MSP systems, PSR J0636+5129 and PSR J1311−3430 (see Draghis & Romani 2018; van Haaften et al. 2012; Romani et al. 2015; Spiewak et al. 2018), are known as the Tidarren (Romani et al. 2016). As a subclass of the BW systems, they have a very low mass companion star and extremely short orbital period (Romani et al. 2016), and their properties are shown in Table 2. The companion stars in the Tidarren systems have strongly heated sides facing the pulsar. This leads to periodic variations in the optical emissions of the system, providing us a means to derive the orbital velocities of the companion stars (see, e.g., Draghis et al. 2019; Kandel et al. 2019). The companion stars of the Tidarren systems have an extremely low mass. Their hydrogen is almost completely stripped, and hence they often appear as helium WDs. The Tidarren systems are therefore more likely to be the progenitors of isolated MSPs than the other subclass of MSP binaries.

The formation of eclipsing MSP systems in the Galactic field is thought to undergo the recycled process similar to the evolution of CV-like low-mass X-ray binaries (Chen et al. 2013; Ginzburg & Quataert 2021). The bimodal distribution of the RBs and BWs can be explained by different evaporation efficiency. However, none of the evolution tracks can match the observed quantities of the Tidarren systems. A different formation mechanism is proposed by King et al. (2003, 2005) that a MSP-WD binary is originally formed in the globular clusters (GCs) and exchanges its companion to a main-sequence star, and is subsequently ejected to the Galactic field, or entered the field populations when their host GCs dissociated (Gnedin & Ostriker 1997). Therefore, we assessed the possibilities of Tidarrens origin by comparing the trajectories of the two systems with the distributions of binaries populations from the Galactic disk or GCs.

All the known Tidarren systems are located at substantial Galactic latitude (with $|b| > 12°$). From their measured distances to Earth, we determined their vertical distances to the Galactic plane z. The z of all Tidarren systems are larger than the scale height of the Galactic thin disk (∼0.12 kpc), and two of them, PSR J1653−0158 and PSR J1311−3430, have z larger than the scale height of the Galactic thick disk (∼0.3 kpc; Jurić et al. 2008; de Jong et al. 2010). Adopting the distance from the Sun to the Galactic center $R_0 = 8$ kpc (see Eisenhauer et al. 2003; Francis & Anderson 2014; Vallée 2017; Camarillo et al. 2018; Griv et al. 2021), we derived the distances of all known Tidarren systems to the Galactic center $R_{\rm C}$ in Table 3. The values of their $R_{\rm C}$ are about 6.6−8.5 kpc, larger than 2 kpc, the radius of the Galactic bulge (see Zoccali & Valenti 2016). We therefore conclude that the currently known Tidarren systems are not in the Galactic bulge or in the Galactic thin disk. A possible explanation for the spatial locations of the Tidarren systems is that they originated from GCs. To examine the scenario that the Tidarren systems were produced in GCs, we first compared the population of BWs and binary MSPs in GCs and in the field. The current version of ATNF Pulsar Catalogue,[10] listed 64 GC binary MSPs and 163 field binary MSPs, and a recent study by Hui & Li (2019) listed 17 BWs in GCs and 29 BWs in field. This gives a ratio of 0.26 for BWs among binary MSPs in GCs and 0.16 for BWs among binary MSPs in the field, consistent with that BWs have no preference to reside in a GC (see, King et al. 2003).

[9] GeV gamma-rays can be produced in the pulsar magnetosphere when low-energy photons are Compton up-scattered by relativistic electrons and positrons (see, e.g., Grenier & Harding 2015).

[10] http://www.atnf.csiro.au/research/pulsar/psrcat

Table 2
Physical Parameters of PSR J1653−0158 and the Other Tidarren Systems

Source	D (kpc)	P (ms)	L_X (10^{31} erg s^{-1})	L_{sd} (10^{33} erg s^{-1})	P_{orb} (day)	M_{com} ($M_\odot$)	M_{NS} [f] ($M_\odot$)	DM (pc cm^{-3})
PSR J1653−0158	0.84[a]	1.97	1.18	4.4	0.052	0.013	1.62	⋯
PSR J0636+5129	0.5[b]	2.8	4.48[c]	5.6	0.066	0.0068	⋯	11.1
PSR J1311−3430	1.4[d]	2.56	5.6	49	0.065	0.011	1.53	37.8

Notes.
[a] The distance of 840 ± 40 pc is obtained from optical modeling (Nieder et al. 2020).
[b] The distance of 0.5 kpc is derived from dispersion measurement (Stovall et al. 2014).
[c] The X-ray luminosity is calculated from power-law modeled flux $15^{+2}_{-7} \times 10^{-13}$ erg cm^{-2} s^{-1} (Spiewak et al. 2016).
[d] The distance of 1.4 kpc is derived from dispersion measurement (Ray et al. 2013).
[e] The minimum pulsar mass is estimated from binary mass function and companion radial velocity amplitude $K = 666.9$ km s^{-1} (J1653−0158), $K = 609.5$ km s^{-1} (J1311−3430). J0636+5129 is the lack of optical radial velocity information (Draghis & Romani 2018; Kaplan et al. 2018; Spiewak et al. 2018).

Table 3
Location and Kinetics of PSR J1653−0158 and the Other Tidarren Systems

Source	R_C (kpc)	l (deg)	b (deg)	z (kpc)	μ_α (mas yr^{-1})	μ_δ (mas yr^{-1})	V_r (km s^{-1})	Ref
PSR J1653−0158	7.28	16.61	24.93	0.36	−19.62 ± 1.86	−3.74 ± 1.12	−174.6 ± 5.1	*a*
PSR J0636+5129	8.46	163.91	18.64	0.16	3.22 ± 0.03	−1.61 ± 0.06	⋯	*b*
PSR J1311−3430	6.89	307.68	28.17	0.79	−6.8 ± 0.6	−3.5 ± 0.8	62.5 ± 4.5	*c*

Note. The references are: *a*. Romani et al. (2014); Nieder et al. (2020); *b*. Stovall et al. (2014); Guillot et al. (2019); *c*. An et al. (2017); Romani et al. (2012). The definitions of the symbols are R_C: distance to Galactic center, adopting the distance from the Sun to the Galactic center $R_0 = 8$ kpc (Camarillo et al. 2018); l: Galactic longitude; b: Galactic latitude; z: distance to the Galactic plane; μ_α, μ_δ: proper motions in R.A. and decl.; V_r: mean radial velocity of the binary system.

Among the three systems listed in Table 3, PSR J1653−0158 and PSR J1311−3430 have both mean radial velocity and proper motion measurements. The orbits of these systems in the Milky Way can therefore be computed. We used `galpy` (Bovy 2015)[11] to track back the orbit of them in the past 1 Gyr.

Figure 5 shows the orbits of PSR J1653−0158 and PSR J1311−3430, and binary populations from the Galactic thin disk or GCs on the $\log R_g$–Z_g/R_g plane, where R_g is the radial distance from the Galactic center, Z_g is the z component of Galactocentric Cartesian coordinate, and $Z_g/R_g = \cos\ \theta$ where θ is the polar angle. The time-averaged absolute values of the Galactic latitude ($\langle|b|\rangle_t$) is 2.°5 for PSR J1653−0158 and 3.°7 for PSR J1311−3430. This gives the time-averaged absolute distances $\langle|z|\rangle_t$ of 0.3 kpc to the Galactic plane for PSR J1653−0158 and of 0.45 kpc for PSR 1311−3430. The time-averaged distances to the Galactic center are 9.7 kpc for PSR J1653−0158 and 8.4 kpc for PSR J1311−3430. As their distances to the Galactic center are larger than 2 kpc, PSR J1653−0158 and PSR J1311−3430 are unlikely associated with the Galactic bulge stellar population. The binary populations in Figure 5 are obtained as follows. We used Monte Carlo methods to sample the binary populations from the Galactic thin disk, where the thin disk assumes a scale height of 0.12 kpc (Rix & Bovy 2013) and a scale length of 4.0 kpc (de Jong et al. 2010), in panel (A) of Figure 5. The GC populations in panel (B) were read directly from the Harris (1996) catalog (2010 edition). Only position information of these populations are shown in panels (A) and (B), and no orbital integration was performed.

For panels (C) and (D), we made further assumptions about the initial velocities for these binary populations, and also about the kick velocities they received. We sampled $N = 10^5$ systems from the Galactic thin disk and $N = 10^5$ systems from GCs, and performed orbital integration of those systems and calculated their time-averaged R_g and Z_g.

For panel (C), the binary population from the Galactic thin disk, their initial velocities on the plane before kicks were calculated following the rotation curve from (Sofue 2017), and the vertical velocity was assumed to be zero. The Maxwellian distribution of the kick velocity is characterized by $\sigma_v = 200$ km s^{-1}, appropriate for the kick received by the binary in the supernova explosion that produced the neutron stars.

For the binary population from GCs in panel (D), the initial 3D velocity follows a Maxwellian distribution (dof = 3). The parameter that determines the distribution was calculated by $\sqrt{3}\,a_1$, where $a_1 = 75.33$ km s^{-1} is the parameter obtained by fitting the radial velocities of GCs with a Maxwellian distribution (dof = 1). We added small kicks with velocities following a Maxwellian distribution with $\sigma_v = 50$ km s^{-1}, corresponding to the recoil velocity of the system when leaving the GC. All the kick velocities are isotropic (evenly distributed over 4π solid angle) in the rest frame of the binaries.

The trajectories of PSR J1653−0158 and PSR J1311−3430 tend to coincide with systems of Galactic disk origins rather than systems of GC origins. For the cases with position information only (without orbital integration), the trajectories of the two systems are consistent with systems of Galactic disk and GC populations. When the kinetic of the systems of the two populations are properly accounted for, the trajectories of PSR J1653−0158 and PSR J1311−3430 are consistent with the expectations from the systems associated with the Galactic disk but inconsistent with the systems associated with GCs. This can be understood as follows. The velocities of the population of systems from the Galactic disk are jointly determined by their rotational motion around the Galactic

[11] `galpy` can be downloaded from http://github.com/jobovy/galpy.

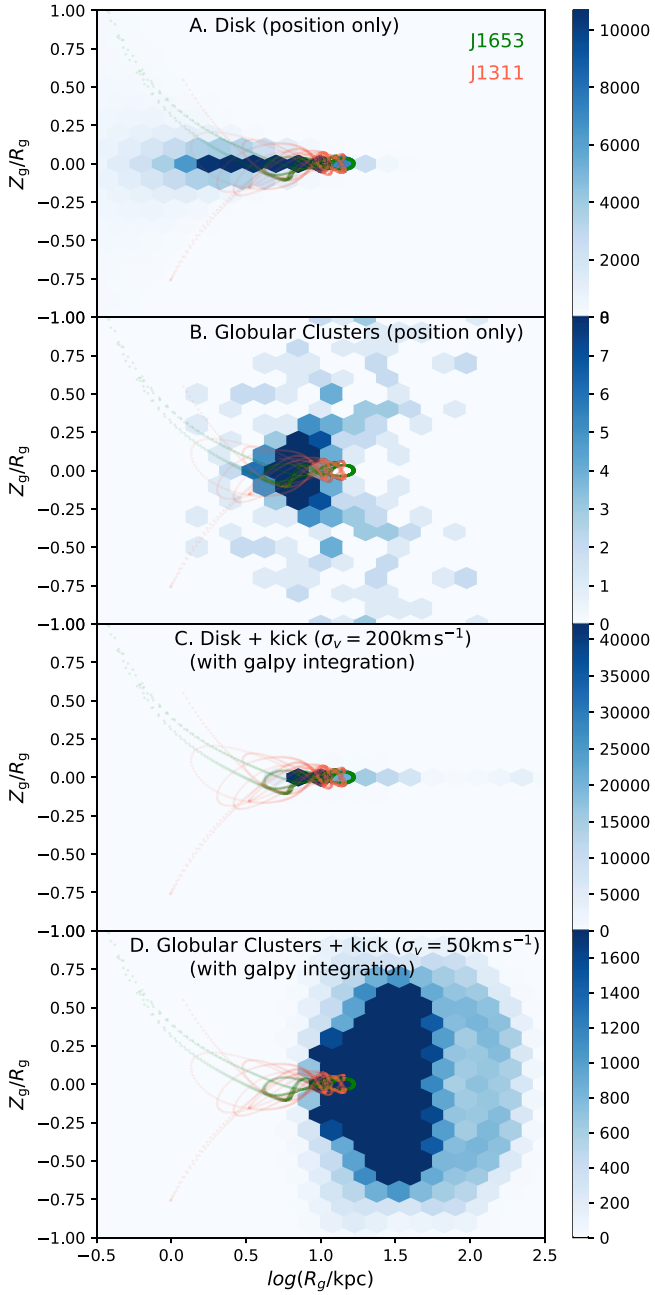

Figure 5. The orbits of PSR J1653−0158 and PSR J1311−3430 in the past 1 Gyr, overlaid with the distributions of binary populations from the Galactic disk or globular clusters (obtained from the catalog or via Monte Carlo simulation). The x and y axes represent the radial distance to the Galactic center (in log R_g) and the polar angle (in Z_g/R_g), respectively. In panels (A) and (C), the positions of binary populations from the Galactic thin disk are sampled with a scale height of 0.12 kpc (Rix & Bovy 2013) and a scale length of 4.0 kpc (de Jong et al. 2010), and in panels (B) and (D), from GCs listed in the Harris (1996) catalog (2010 edition). Systems in panels (A) and (B) do not receive a kick at birth. Systems in panels (C) and (D) received a kick, which has an isotropic Maxwellian velocity distribution with $\sigma_v = 200$ km s^{-1} and 50 km s^{-1}, respectively.

center and their kick velocity. Among the two velocities, the rotation component does not affect the time-averaged positions of the systems during orbital integration, and it also dilutes the effects brought by the kick velocity. For the population of systems from GCs, the kick velocity is relatively small, and the movements were determined by the (3D) velocities of GCs. In our calculations, the velocities of GCs were derived from radial velocities provided by the GC catalog, and a significant fraction of the systems have relatively large radial velocities in the Galactocentric coordinate. This introduces substantial scatters toward larger R_g in the distribution, which is at odds with the expected locations of PSR J1653−0158 and PSR J1311−3430 from their computed past trajectories. In summary, our kinematic analyses have shown that PSR J1653−0158 and PSR J1311−3430 are more likely to have originated from the Galactic disk rather than GCs.

5. Conclusion

We presented a broadband timing and spectral analysis of the BW MSP binary PSR J1653−0158 using XMM-Newton, NuSTAR, and Fermi-LAT data. Our analysis did not reveal detectable periodic modulations in the 0.2–40 keV energy band. The null detection of the binary orbital modulation could be due to the substantial background contribution to the photon counts. We found that the X-ray spectrum can be modeled by an absorbed power law, with the best-fit photon index $\Gamma = 1.71 \pm 0.09$, (spectral index $\alpha = 0.71 \pm 0.09$), a value typical of optically thin synchrotron radiation from electrons freshly accelerated in shocks via stochastic processes. The unabsorbed X-ray flux, up to 40 keV was determined to be $1.40^{+0.13}_{-0.12} \times 10^{-13}$ erg cm^{-2}s^{-1}, implying an X-ray luminosity of 1.18×10^{31} erg s^{-1} for a distance of 0.84 kpc derived from the optical observations. We examined if the X-ray emission would be contributed by the pulsar atmospheric emissions. The addition of a neutron star atmosphere component to the absorbed power-law spectrum gave a photon index of $\Gamma = 1.60 \pm 0.15$. However, this additional spectral component is not statistically significant.

We modeled the combined X-ray and gamma-ray spectra of PSR J1653−0158 with an intrabinary shock and magnetospheric emission model. The intrabinary shock is formed when the pulsar wind collides with the media ablated from the semidegenerate companion, and the synchrotron X-rays are emitted from the electrons accelerated by the shock. The gamma-rays are produced by curvature radiation from energetic charged particles in the pulsar magnetosphere.

The origin of PSR J1653−0158 and its similar systems were discussed. We grouped the BW systems with extremely low mass companion stars and extremely short orbital periods as the Tidarren systems and conducted an analysis of their spatial location in the Milky Way and their kinetic properties. We found that these Tidarren systems have radial distances $R_C \sim 6.6$−8.5 kpc to the Galactic center and vertical distances $z \sim 0.16$−0.79 kpc to the Galactic plane, implying that they are not currently located in the Galactic bulge or the Galactic thin disk.

The possibilities that the two Tidarren systems originated from the Galactic disk or GCs were assessed using their computed trajectories from `galpy` in the past 1 Gyr. Their trajectories indicated that PSR J1653−0158 and PSR J1311−3430 have been residing within a radial distance of ∼16 kpc from the Galactic center. PSR J1653−0158 had a time-averaged distance of 9.7 kpc to the Galactic center and a time-averaged distance of 0.3 kpc from the Galactic plane. PSR J1311−3430 had a time-averaged distance of 8.4 kpc to the Galactic center and a time-averaged distance of of 0.45 kpc from the Galactic plane. We further conducted a more detailed kinematic analysis of the populations of similar compact binaries, assuming origins from the Galactic disk and GCs.

Comparing their distributions with the computed past trajectories of PSR J1653−0158 and PSR J1311−3430 suggests that the two Tidarren systems are likely marked to have originated in the Galactic disk.

We thank the referee for the critical comments and useful suggestions that led to substantial improvement of the science of this work. This work is supported in part by the Ministry of Science and Technology of Taiwan (ROC) under the grants 109-2628-M-007-005-RSP and 110-2628-M-007-005 (PI: A. Kong). K.W. is supported in part by a UK STFC Consolidated Grant to UCL-MSSL. J.T. acknowledges the support by National Key R&D Program of China, 2020YFC2201400, NSFC U1838102. C.Y.H. is supported by the National Research Foundation of Korea through grants 2016R1A5A1013277 and 2019R1F1A1062071. K.L. L. is supported by the Ministry of Science and Technology of Taiwan (ROC) through grant 109-2636-M-006-017, and by the Ministry of Education of Taiwan (ROC) through a Yushan (Young) Scholarship. Analyses conducted by Q.H. at UCL-MSSL were supported by a UCL Overseas Research Scholarship and a UK STFC PhD Studentship. This work has made use of NASA's Astrophysics Data System and the CSIRO ATNF Pulsar Catalogue (Manchester et al. 2005). The updated list of eclipsing spider MSP binaries in the Galactic field is provided by Jane Yap.

Software: XSPEC (v12.11; Arnaud 1996), SAS (v19.0; Gabriel et al. 2004), NUSTARDAS (v1.9.6; Harrison et al. 2013), Fermitools (Fermi Science Support Development Team 2019), make4FGLxml.py, galpy (Bovy 2015).

ORCID iDs

Jane SiNan Long https://orcid.org/0000-0002-2126-0050
Albert K. H. Kong https://orcid.org/0000-0002-5105-344X
Kinwah Wu https://orcid.org/0000-0002-7568-8765
Qin Han https://orcid.org/0000-0002-2342-9956
David C. Y. Hui https://orcid.org/0000-0003-1753-1660
Kwan Lok Li https://orcid.org/0000-0002-0439-7047

References

Abbott, B. P., Abbott, R., Abbott, T. D., et al. 2018, PhRvL, 121, 161101
Abdollahi, S., Acero, F., Ackermann, M., et al. 2020, ApJS, 247, 33
Achterberg, A., Gallant, Y. A., Kirk, J. G., & Guthmann, A. W. 2001, MNRAS, 328, 393
An, H., Romani, R. W., Johnson, T., Kerr, M., & Clark, C. J. 2017, ApJ, 850, 100
Arnaud, K. A. 1996, in ASP Conf. Ser. 101, Astronomical Data Analysis Software and Systems V, ed. G. H. Jacoby & J. Barnes (San Francisco, CA: ASP), 17
Bell, A. R. 1978, MNRAS, 182, 147
Bhattacharya, D., & van den Heuvel, E. P. J. 1991, PhR, 203, 1
Bovy, J. 2015, ApJS, 216, 29
Camarillo, T., Mathur, V., Mitchell, T., & Ratra, B. 2018, PASP, 130, 024101
Chen, H.-L., Chen, X., Tauris, T. M., & Han, Z. 2013, ApJ, 775, 27
Cheng, K. S., Ho, C., & Ruderman, M. 1986, ApJ, 300, 500
de Jong, J. T. A., Yanny, B., Rix, H.-W., et al. 2010, ApJ, 714, 663
Draghis, P., & Romani, R. W. 2018, ApJL, 862, L6
Draghis, P., Romani, R. W., Filippenko, A. V., et al. 2019, ApJ, 883, 108
Dyks, J., & Rudak, B. 2003, ApJ, 598, 1201
Eisenhauer, F., Schödel, R., Genzel, R., et al. 2003, ApJL, 597, L121
Faucher-Giguére, C.-A., & Kaspi, V. M. 2006, ApJ, 643, 332
Francis, C., & Anderson, E. 2014, MNRAS, 441, 1105
Fruchter, A. S., Stinebring, D. R., & Taylor, J. H. 1988, Natur, 333, 237
Gabriel, C., Denby, M., Fyfe, D. J., et al. 2004, in ASP Conf. Ser. 314, Astronomical Data Analysis Software and Systems (ADASS) XIII, ed. F. Ochsenbein, M. G Allen, & D. Egret (San Francisco, CA: ASP), 759
Ginzburg, S., & Quataert, E. 2021, MNRAS, 500, 1592
Gnedin, O. Y., & Ostriker, J. P. 1997, ApJ, 474, 223
Grenier, I. A., & Harding, A. K. 2015, CRPhy, 16, 641
Griv, E., Gedalin, M., Pietrukowicz, P., Majaess, D., & Jiang, I.-G. 2021, MNRAS, 502, 4194
Guillot, S., Kerr, M., Ray, P. S., et al. 2019, ApJL, 887, L27
Harris, W. E. 1996, AJ, 112, 1487
Harrison, F. A., Craig, W. W., Christensen, F. E., et al. 2013, ApJ, 770, 103
Heinke, C. O., Rybicki, G. B., Narayan, R., & Grindlay, J. E. 2006, ApJ, 644, 1090
Huang, R. H. H., Kong, A. K. H., Takata, J., et al. 2012, ApJ, 760, 92
Hui, C. Y., & Li, K. L. 2019, Galax, 7, 93
Hui, C. Y., Park, S. M., Hu, C. P., et al. 2015, ApJ, 809, 68
Hui, C. Y., Wu, K., Han, Q., Kong, A. K. H., & Tam, P. H. T. 2018, ApJ, 864, 30
Iben, I., Tutukov, A. V., & Fedorova, A. V. 1997, ApJ, 486, 955
Jia, K., & Li, X. D. 2014, ApJ, 791, 127
Jurić, M., Ivezić, Ž., Brooks, A., et al. 2008, ApJ, 673, 864
Kandel, D., Romani, R. W., & An, H. 2019, ApJ, 879, 73
Kaplan, D. L., Stovall, K., van Kerkwijk, M. H., Fremling, C., & Istrate, A. G. 2018, ApJ, 864, 15
Kiel, P. D., & Taam, R. E. 2013, Ap&SS, 348, 441
King, A. R., Beer, M. E., Rolfe, D. J., Schenker, K., & Skipp, J. M. 2005, MNRAS, 358, 1501
King, A. R., Davies, M. B., & Beer, M. E. 2003, MNRAS, 345, 678
Kluzniak, W., Ruderman, M., Shaham, J., & Tavani, M. 1988, Natur, 334, 225
Kong, A. K. H., Jin, R., Yen, T. C., et al. 2014, ApJL, 794, L22
Kong, A. K. H., Takata, J., Hui, C. Y., et al. 2018, MNRAS, 478, 3987
Lattimer, J. M., & Prakash, M. 2001, ApJ, 550, 426
Li, K. L., Kong, A. K. H., Takata, J., et al. 2014, ApJ, 797, 111
Lomb, N. R. 1976, Ap&SS, 39, 447
Manchester, R. N., Hobbs, G. B., Teoh, A., & Hobbs, M. 2005, AJ, 129, 1993
Nieder, L., Clark, C. J., Kandel, D., et al. 2020, ApJL, 902, L46
Papitto, A., Ferrigno, C., Bozzo, E., et al. 2013, Natur, 501, 517
Phinney, E. S., Evans, C. R., Blandford, R. D., & Kulkarni, S. R. 1988, Natur, 333, 832
Ray, P. S., Ransom, S. M., Cheung, C. C., et al. 2013, ApJL, 763, L13
Rix, H.-W., & Bovy, J. 2013, A&ARv, 21, 61
Roberts, M. S. E. 2013, in IAU Symp. 291, Neutron Stars and Pulsars: Challenges and Opportunities after 80 years, ed. J. van Leeuwen (Cambridge: Cambridge Univ. Press), 127
Romani, R. W., Filippenko, A. V., & Cenko, S. B. 2014, ApJL, 793, L20
Romani, R. W., Filippenko, A. V., & Cenko, S. B. 2015, ApJ, 804, 115
Romani, R. W., Filippenko, A. V., Silverman, J. M., et al. 2012, ApJL, 760, L36
Romani, R. W., Graham, M. L., Filippenko, A. V., & Zheng, W. 2016, ApJ, 833, 138
Ruderman, M., Shaham, J., & Tavani, M. 1989, ApJ, 336, 507
Rybicki, G. B., & Lightman, A. P. 1986, Radiative Processes in Astrophysics (New York: Wiley)
Scargle, J. D. 1982, ApJ, 263, 835
Sofue, Y. 2017, PASJ, 69, R1
Spiewak, R., Bailes, M., Barr, E. D., et al. 2018, MNRAS, 475, 469
Spiewak, R., Kaplan, D. L., Archibald, A., et al. 2016, ApJ, 822, 37
Stappers, B. W., Bailes, M., Lyne, A. G., et al. 1996, ApJL, 465, L119
Stovall, K., Lynch, R. S., Ransom, S. M., et al. 2014, ApJ, 791, 67
Takata, J., Cheng, K. S., & Taam, R. E. 2012, ApJ, 745, 100
Vallée, J. P. 2017, Ap&SS, 362, 79
van Haaften, L. M., Nelemans, G., Voss, R., & Jonker, P. G. 2012, A&A, 541, A22
Wang, Y., Takata, J., & Cheng, K. S. 2011, MNRAS, 414, 2664
Watters, K. P., Romani, R. W., Weltevrede, P., & Johnston, S. 2009, ApJ, 695, 1289
Zoccali, M., & Valenti, E. 2016, PASA, 33, e025